Abnormal magnetic behavior of prussian blue analogs modified with multi-walled carbon nanotubes

Jia-Jun Mo(莫家俊)[1], Pu-Yue Xia(夏溥越)[1], Ji-Yu Shen(沈纪宇)[1], Hai-Wen Chen(陈海文)[2], Ze-Yi Lu(陆泽一)[1], Shi-Yu Xu(徐诗语)[1], Qing-Hang Zhang(张庆航)[1], Yan-Fang Xia(夏艳芳)[1,†], and Min Liu(刘敏)[1,‡]

[1] *College of Nuclear Science and Technology, University of South China, Hengyang* 421001, *China*
[2] *College of Energy, Xiamen University, Xiamen* 361005, *China*

(Received 26 July 2022; revised manuscript received 21 September 2022; accepted manuscript online 23 September 2022)

This work examines the origin of the abnormal magnetism exhibited by CuMnFe–PBAs modified with multi-walled carbon nanotubes (MWCNTs). The system of CuMnFe–PBAs@MWCNTs coexists with both large and small clusters. CuMnFe–PBAs clusters have an average particle size of 28 nm, and some of the smaller particles are adsorbed on the surface of MWCNTs. Surprisingly, the magnitude of magnetization increases linearly with decreasing temperature. When above the Curie temperature, the magnitude of magnetization is significantly greater than that of PBAs without being modified. This phenomenon can be attributed to magnetostatic interactions between ultra-fine magnetic nanoparticles adsorbed on the surface of MWCNTs. Using the Monte Carlo method, we simulated the magnetostatic interaction of cylindrical adsorbed particles, and the simulation results are almost identical to those observed experimentally. The results indicate that 0.089 CuMnFe–PBAs clusters per 1 nm^2 can be adsorbed onto the surface area of MWCNTs. We demonstrate that MWCNTs adsorbing magnetic particles exhibit magnetic behavior, and suggest a method for producing ultrafine materials. It also introduces a new method of calculating the adsorption efficiency of carbon nanotubes, offering theoretical guidance for future research on nanomaterials with enhanced adsorption efficiency.

Keywords: multi-walled carbon nanotubes, prussian blue analogue, Monte Carlo simulation, magnetostatic interaction

PACS: 75.50.–y, 75.75.–c, 76.80.+y, 02.70.Uu **DOI:** 10.1088/1674-1056/ac946b

1. Introduction

Multi-walled carbon nanotube (MWCNT) possesses a number of unique properties[1–4] such as low density, high specific surface area, high tensile strength, high adsorption capacity, and high electrical conductivity. Via pairing and offsetting electrons,[5,6] a zero moment is created, thus resulting in diamagnetism. MWCNTs have been the subject of numerous reports in recent years. Likodimos *et al.* studied the magnetic properties of MWCNTs,[7] discovering an increase in diamagnetic susceptibility at low temperatures, and it is confirmed that there is an optical Aharonov–Bohm (AB) effect in the quantum ring of MWCNTs. Chang *et al.* presented a variety of magnetic resonance spectra of MWCNTs, and attributed the magnetism of carbon nanotubes to coupling between the free spins of dangling bonds, which also results in weak ferromagnetism coupling.[8] Simultaneously, the improvements of properties have been verified in materials modified by MWCNTs.[9,10]

Prussian blue analogues (PBAs) have a crystal structure similar to that of metal–organic skeleton (MOF). Its structure is like NaCl, and two adjacent ions are connected by one cyano. PBAs have long been applied in the fields of electricity, magnetism, catalysis, *etc.*[11–20] However, a number of disadvantages such as easy particle agglomeration, low conductivity, easy structure collapse, and poor wettability have been widely reported, which all result from low electron transport rate, poor cycle stability, and lower active center utilization.[21] To overcome these defects, it is necessary to handle PBAs with some special means, among which is compounding with other substances.

Composite materials own the characteristic advantages of their constituent materials and can sometimes exhibit complementary properties. Different materials modified with PBAs and MWCNTs can exhibit significant improvements in their properties, particularly in electrochemistry.[22] Because of its high stability and high ion load, it has been widely used in the treatment and adsorption of heavy metals and nuclear wastes and sensing devices.[23]

In this paper, we compare the magnetic properties of $Cu_{0.64}Mn_{0.86}[Fe(CN)_6]$ (CuMnFe–PBAs) modified with multi-walled carbon nanotubes to those unmodified. Mössbauer spectra are used to determine whether the modification of MWCNTs can affect the chemical properties and coordination environment of PBAs. Also, Monte Carlo simulations based on magnetostatic interactions are applied to investigate the magnetic mechanism.

†Corresponding author. E-mail: xiayfusc@126.com
‡Corresponding author. E-mail: liuhart@126.com

© 2023 Chinese Physical Society and IOP Publishing Ltd

2. Methods

2.1. Synthesis of materials

The whole experimental preparation scheme is divided into the control and experimental parts. CuMnFe–PBA without MWCNTs is the control group (CG–PBA), and CuMnFe–PBA modified by MWCNTs is the experimental group (EG–PBA).

2.1.1. The control group

The mixture solution of 100-mL $K_3Fe(CN)_6$ (16 mmol), 200 mL $CuSO_4$ (6.84 mmol), and $MnSO_4$ (9.06 mmol) was treated by sonicating for 6 hours and standing overnight. The supernatant was removed, and the sediment was filtered to obtain a light brown precipitate. The precipitation was washed with 0.1-mol/L HCl, rinsed with clean water, and washed again with 0.1-mol/L NaOH until the yellowish precipitation was removed entirely. Finally, the precipitation filtrate was rinsed several times with HCl (pH = 2) and water, followed by the air dry for several hours at room temperature.

2.1.2. The experimental group

To begin, the MWCNTs are purified and opened using concentrated sulfuric acid, and experience the following steps:

(i) 0.4-g unpurified MWCNTs were placed in a small beaker containing 400-ml H_2SO_4 (1:3) solution and treated with ultrasound at 50 °C for six hours.

(ii) The black suspension was diluted with 100 ml of deionized water and left overnight to precipitate.

(iii) The suspension is diluted and filtered again with deionized water after removing the supernatant.

(iv) The precipitate was washed with 0.1-mol/L NaOH solution twice to remove impurity fragments.

(v) HCl with the concentration of 0.1 mol/L was used to wash the precipitate until the filtrate is neutral.

(vi) The precipitation was dried at 120 °C for 4 hours.

After pretreatment and purification, 83-mg MWCNTs were added to a solution of 3.7-mmol $CuSO_4$ (0.0128 mol/L, 290 mL) and 4.7-mmol $MnSO_4$ (0.0162 mol/L, 290 mL) for a 6-hour ultrasonic treatment, and the precipitate was obtained by filtration. 98.775-mg $K_3Fe(CN)_6$ solution (0.03 mol/L, 10 mL) was added to the precipitate and left for one night to ensure a complete reaction. The light brown precipitate CuMnFe–PBAs@MWCNTs were obtained by filtration, followed by the repeated wash with 0.01-mol/L HCl, water, and 0.01-mol/L NaOH solution until the light yellow disappears. Then the obtained sample was filtered and washed with HCl (pH = 2) and water, and conducted air dry for several hours at room temperature. Finally, $Cu_{0.64}Mn_{0.86}[Fe(CN)_6]$ @MWCNTs were obtained as the target product.

2.2. Measurement method

2.2.1. X-ray diffraction

X-ray diffraction (XRD) uses Siemens D500 Cu $K\alpha$ (λ = 1.5418 Å) diffractometer at a rate of 0.02°/s within the range of 20° to 80°. The obtained data were processed with MDI Jade 9.0 software.

2.2.2. Mössbauer spectrum

The transmission ^{57}Fe Mössbauer spectrum were collected at room temperature (RT) on SEE Co W304 Mössbauer spectrometer with a ^{57}Co/Rh source in transmission geometry equipped in a cryostat (Advanced Research Systems, Inc.,4K). The data results were handled with MössWinn 4.0 software to fit parameters such as isomer shifts (ISs), quadrupole splitting (QS), *etc.*

2.2.3. Magnetic measurements

The *M versus H* is measured under an external magnetic field ranging from −7 T to 7 T at the temperature of 5 K. The measurement of magnetization dependent on temperature from 5 K to 300 K is made at an external magnetic field of 100 Oe (1 Oe = 79.5775 A·m^{-1}).

3. Results and discussion

3.1. Elemental and component analysis

The results of EG–PBA indicate the elemental composition (%) is C: 16.83, N: 19.33, and H: 3.23, and that (%) of CG–PBA is C: 60.31, N: 4.09, and H: 2.256. That is to say, $n(H_2O)$:n(CuMnFe–PBAs) equals 7.90:1. The rate of MWCNTs and CuMnFe–PBAs can be inferred using extrapolation of the C/N ratio from elemental analysis. It is calculated that $n(\text{MWCNTs}) = n(\text{CuMnFe}-\text{PBAs}) = 97.29{:}1$ and $n(H_2O) = n(\text{CuMnFe}-\text{PBAs}) = 23.16{:}1$, which can be used to calculate the molar magnetic susceptibility. It is worth noting that the increased water molecule content could be explained by water molecules being accommodated within the interlaced spaces between MWCNTs, thus forming water molecular films on their surfaces. The result of x-ray fluorescence spectrometry indicates that the radioactivity of the control group and experimental group metal elements (Fe, Mn, and Cu) are 0.636:0.853:1.024 and 0.642:0.861:0.997, respectively. Chemical formulas of $Cu_{0.64}Mn_{0.86}[Fe(CN)_6]\cdot 6.9H_2O$ and $Cu_{0.64}Mn_{0.86}[Fe(CN)_6]@97.3C\cdot 23.2H_2O$ for CG–PBA and EG–PBA, respectively are also inferred from it.

3.2. X-ray diffraction and scanning electron microscopy

The XRD spectrum of EG–PBA and CG–PBA is shown in Fig. 1(a). Based on the standard PDF cards installed on Jade 9.0 software, both samples are face-centered cubic structures belonging to the Fm-3m space group. The XRD results of

the experimental group are consistent with expectations. The absence of diffraction peak separation in the CuMnFe–PBAs phase demonstrates that each phase of the sample is mainly composed of one single component. The lattice constant of EG–PBA and CG–PBA are 10.12305 Å and 10.132145 Å respectively. In addition, the marked MWCNTs phase can be observed, indicating that the synthetic result of the sample is satisfactory.

Figure 1(b) exhibits the TEM of EG–PBA. It shows that the PBA clusters are loaded onto the surface of the MWCNT, indicating that the adsorption of PBAs by MWCNTs was successfully achieved. MWCNTs have a diameter of 6 nm–10 nm, and the thickness of CuMnFe–PBAs adsorbed on their surface is approximately 1–2 times longer than their diameters. MWCNTs are textured at the hundred-nanometer scale of TEM, and some large CuMnFe–PBAs clusters in the EG–PBA system are bound by the texture of MWCNTs. It is unlikely to rule out the possibility that clusters are formed by the shedding of the surface of MWCNTs or are deposited by the texture of MWCNTs binding. Also, we quantify the dimensions of the large CuMnFe–PBAs clusters in the EG–PBA system as illustrated in Fig. 1(c). The particle size was calculated using Nano Measurer software. The size statistics of large CuMnFe–PBA clusters follow a logarithmic normal distribution with parameters of $\sigma = 0.446$, $\mu = 3.265$, and the mean diameter is ~ 28.9 nm.

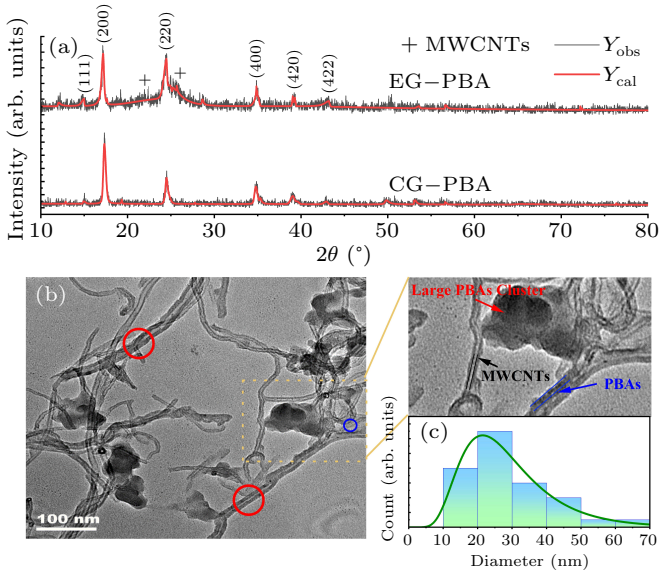


Fig. 1. The characterization results of CuMnFe–PBAs modified with MWCNTs. (a) The x-ray diffraction spectra of EG–PBA and CG–PBA. (b) Transmission electron microscope (TEM) micrograph of EG–PBA, where red circles display the morphology and the blue circle shows the morphology with no or fewer PBAs adsorbed by MWCNTs. (c) The size distribution of some free CuMnFe–PBAs clusters in EG–PBA.

3.3. Mössbauer spectrum

Mössbauer spectroscopy is a useful tool for investigating magnetic orders, ambient interactions, and surrounding conditions of Mössbauer nuclei. Our objective here is to study the chemical properties of Prussian blue analogs before and after being modified by MWCNTs with the help of Mössbauer spectroscopy. Figure 2 shows the Mössbauer spectra fitting result. The parameters obtained through fitting are listed in Table 1. According to the fitting results of the Mössbauer spectra, the system contains two coordination environments around Fe nuclei, so a singlet and a doublet appear concurrently in the analysis. In general, the doublet is caused by low-spin Fe^{III} ($S = 1/2$) with two antiparallel electron spins and isolated spin orientations in t_{2g} orbits, thus resulting in an asymmetric crystal field. Isolated electrons generate an electric field gradient which prevents the Fe^{III} nucleus from having a spherically symmetric charge distribution, so a non-zero quadrupole splitting (QS) appears. When the Fe^{II} low-spin atoms are in symmetrical octahedral–CN–coordination spheres, electrons are paired in t_{2g} orbits with no electric field gradient, so the QS is zero and appears a singlet. The coexistence of singlet and doublet observed here is due to charge transfer between Cu^{II}/Mn^{II} and Fe^{III} via cyanide bridging. When electrons transfer to Fe^{III}, the origin ions turn into Fe^{II}. The radio of singlet and doublet is 13.9% and 86.1% in CG–PBA, and 12.4% and 87.6% in EG–PBA, respectively. The areas of singlet and doublet remained basically unchanged following MWCNT modification. This indicates that the charge transfer phenomenon originates from the CuMnFe–PBAs system itself, and the modification of MWCNTs fails to affect it directly. It is worth noting that the QS of doublet of EG–PBA is greater than that of CG–PBA, which is attributed to the size effect,[24] *i.e.*, CuMnFe–PBAs@MWCNTs have a higher surface-to-volume ratio, resulting in a greater lattice strain and electric field gradient. It is consistent with the TEM characterization results above. The value of isomer shift (IS) reflects the density of s-orbit electron clouds around Fe nuclei. MWCNTs did not undergo significant changes in their chemical environment or properties in the course of modification as evidenced by their little-changed value of IS. In this regard, PBAs modified by MWCNTs can hardly undergo changes in their chemical properties.

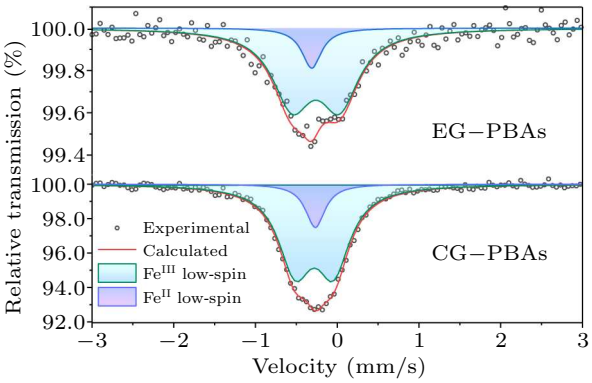


Fig. 2. The Mössbauer spectra of CuMnFe–PBA@MWCNTs and CuMnFe–PBAs.

Table 1. The Mössbauer spectra parameters of EG–PBA and CG–PBA.

Sample		IS (mm/s)	QS (mm/s)	Area (%)
EG–PBA	Singlet	−0.31	–	12.4
	Doublet	−0.26	0.58	87.6
CG–PBA	Singlet	−0.26	–	13.9
	Doublet	−0.28	0.47	86.1

3.4. Magnetic measurements

Figure 3 presents the magnetic behavior of EG–PBA and CG–PBA. The magnetization curve of CG–PBA exhibits significant magnetic hysteresis, and the coercivity is approximately 0.8 kOe as illustrated in Fig. 3(a). The magnetization curve of EG–PBA exhibits a slight positive transverse axis shift, which may be due to the exchange bias effect caused by the compensated antiferromagnetic spin on the surface of CuMnFe–PBAs.[25] It is worth noting that when CuMnFe–PBAs are modified by MWCNTs, their coercivity decreases significantly in comparison with CG–PBA. Meanwhile, the magnetization of EG–PBA exhibits a slight response to applied magnetic fields. They do not reach saturation when subjected to a strong field. The magnetization curves of CG–PBA exhibit an approximately linear relationship, which is the characteristic of antiferromagnetism. However, under a high field, the magnetization of EG–PBA is nonlinear, and the magnetization curve resembles to be a paramagnetic behavior. The magnetization curve can be described using the famous Langevin function (Fig. 3(a), red line).

$$\frac{M}{M_S} = \coth\left(\frac{\mu_{\text{eff}}H}{k_B T}\right) - \frac{k_B T}{\mu_{\text{eff}}H}, \tag{1}$$

where the saturation magnetization is denoted by M_S, H is the external magnetic field, k_B denotes the Boltzmann constant, and μ_{eff} represents the effective magnetic moment. The experimental data are consistent with the theoretical value, indicating that the system exhibits superparamagnetic behavior. Due to the small radius of MWCNTs ($r_{\text{MWCNTs}} \sim 8$ nm), PBAs will be adsorbed on their surface, significantly reducing the particle size of PBAs. Small clusters with no fixed magnetic orientation are unconstrained by thermal perturbation, resulting in a superparamagnetic effect similar to paramagnetic behavior, as illustrated in Fig. 4. When a magnetic nanoparticle attains a superparamagnetic state, it undergoes a superparamagnetic relaxation process, during which its magnetization direction rapidly fluctuates rather than remaining fixed in one direction. Thermal activation overcomes the magnetic anisotropy energy barrier of a nanoparticle, causing it to become superparamagnetically relaxed. The saturation magnetization and effective magnetic moment are calculated as 4.06 μ_B and 5.20 μ_B respectively. The theoretical value of μ_{eff} is

$$\mu_{\text{eff}} = 2R \times \sqrt{1\cdot S_{\text{Fe}}(S_{\text{Fe}}+1) + 0.86\cdot S_{\text{Mn}}(S_{\text{Mn}}+1) + 0.64\cdot S_{\text{Cu}}(S_{\text{Cu}}+1)}, \tag{2}$$

where $S_{\text{Fe}} = 1/2$, $S_{\text{Mn}} = 5/2$, and $S_{\text{Cu}} = 1/2$. R denotes the radio contribution of Fe^{III} to the total system (derived from Mössbauer fitting result and equal to 0.88); the magnetic contribution of the Fe^{II} system is close to zero. The μ_{eff} is calculated to be 5.21 μ_B, which agrees well with the result of the Langevin function fitting. The magnetization *versus* temperature is illustrated in Figs. 3(b) and 3(c). The magnetization of EG–PBA decreases linearly with increasing temperature. It has no discernible phase transition temperature above 5 K, which is due to the size effect. Between 5 K and 20 K, magnetization rapidly decreases, but the decline slows after 20 K. Despite this, it does not attain the paramagnetic state and retains a higher magnetization at higher temperatures; this phenomenon is also observed in Refs. [26,27], and can be attributed to magnetostatic interaction Refs. [28–32]. In comparison, the magnetization of CG–PBA is clearly paramagnetic when $T > T_C$ and ferromagnetic when $T < T_C$. However, the Mössbauer spectra results indicate that the charge distribution surrounding the Fe nucleus did not change significantly before and after the addition of MWCNTs, indicating that the exchange coupling mechanism of the system remained unchanged. Magnetostatic interaction is critical in this system for the magnetic properties of EG–PBA.

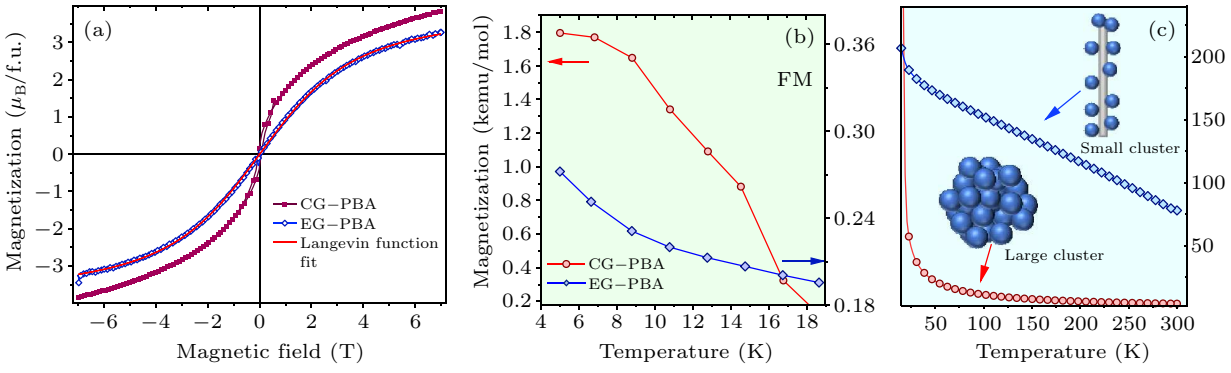


Fig. 3. The magnetization of CG–PBA and EG–PBA. (a) *M versus H* plot for CG–PBA and EG–PBA at 5 K. The inset shows in detail of the low field behavior of $M(H)$. The magnetizations at low and high temperatures for EG–PBA and CG–PBA are measured under an external field of 100 Oe. (b) The magnetization of ferromagnetic behavior at low temperature. (c) The paramagnetic behavior at high temperature.

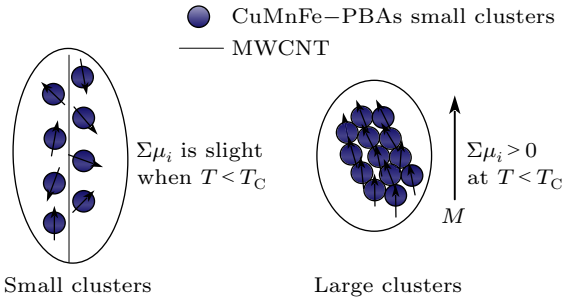


Fig. 4. Diagram of magnetic moment orientation distribution of the small clusters attached to MWCNTs and that of free large clusters.

4. Theoretical calculation and Monte Carlo simulation

To shed light on the mechanism underlying the magnetic properties of CuMnFe–PBAs@MWCNTs in the paramagnetic region, we developed a model of dipolar interaction and ran Monte Carlo (MC) simulations. It can be assumed that the CuMnFe–PBAs adsorbed on MWCNTs are single domain clusters. Magnetic ions in a single domain molecule all have the same magnetic moment. As shown in Fig. 5, we created a tubular space to fully simulate the spatial distribution of PBAs adsorption on MWCNTs. The diameter of one MWCNT d_C is set as 8 nm, and the average particle size $\overline{d_P}$ is $1.5d_C$. The particle size obeys logarithmic normal distribution, and let the parameter μ_S and σ_S as $\mu_S = \ln(\overline{d_P})$, $\sigma_S = (\sigma/\mu)\mu_S$ (suppose that the coefficient of variance of large CuMnFe–PBAs clusters is the same as that of PBAs adsorbed on MWCNTs, *i.e.*, $\sigma/\mu = \sigma_S/\mu_S$), where $\sigma = 0.446$, and $\mu = 3.265$ are calculated by the size distribution of large CuMnFe–PBAs clusters. The generated size obeys lognormal distribution, *i.e.*,

$$p(v,\mu_v,\sigma_S) = \frac{1}{\sqrt{2\pi}\sigma_S v}\exp\left[-\frac{\ln(v-\mu_v)}{2\sigma_S}\right], \tag{3}$$

where, $v = \pi/6d^3$, $\mu_v = 3\mu_S + \ln(\pi/6)$. In the constrained space, the PBA clusters will be randomly distributed uniformly, and a large number of single domain clusters will be adsorbed on the surface of MWCNT. Certain clusters, such as the red ball in Fig. 5, may be unable to contact the surface of MWCNTs.

The energy of the whole system can be composed of three parts, the first energy term is the anisotropic energy E_A, *i.e.*,

$$E_A = -K\sum_i \left(\frac{\boldsymbol{\mu}_i\cdot\boldsymbol{n}_i}{|\boldsymbol{\mu}_i|}\right)^2, \tag{4}$$

where K represents the anisotropic constant, $\boldsymbol{n}_i$ donates the random unit vector, $\boldsymbol{\mu}_i$ is the magnetic moment vector and $|\boldsymbol{\mu}_i| = M_S V_i$. Herein, M_S is the saturation magnetization, which is independent on temperature, V_i is the volume of the i-th particle. The second term is dipole–field interaction energy E_H,

$$E_H = -\sum_i \boldsymbol{\mu}_i\cdot\boldsymbol{H}, \tag{5}$$

where $\boldsymbol{H}$ is the external field vector. This term shows the magnetization dependent on the external field, and the vary law is obey the Langevin function, when the particle is the superparamagnetic particle. The third term is the dipole–dipole interaction, which describes the origin of net magnetization, and the dipole–dipole interact energy E_D is

$$E_D = \frac{\mu_0}{4\pi}\sum_i\sum_{j\neq i}\frac{\boldsymbol{\mu}_i\cdot\boldsymbol{\mu}_j}{r_{ij}^3} - \frac{3(\boldsymbol{\mu}_i\cdot\boldsymbol{r}_{ij})(\boldsymbol{\mu}_j\cdot\boldsymbol{r}_{ij})}{r_{ij}^5}, \tag{6}$$

where μ_0 is the vacuum permeability, $\boldsymbol{r}_{ij}$ is a distance vector joining the centers between the i-th and j-th clusters. The total energy E of the system is the superposition of the above three energies, *i.e.*,

$$E = E_A + E_D + E_H. \tag{7}$$

We use the Monte Carlo method to simulate the magnetic behavior of the CuMnFe–PBAs cluster absorbed on the surface of MWCNTs. Under the thermal disturbance, each single-domain cluster randomly flips. The flip probability P is based on the Metropolis–Hasting criterion[33,34]

$$P = \frac{-\Delta E}{k_B T}. \tag{8}$$

In the process of Monte Carlo simulation, we randomly select a particle, calculate its energy difference ΔE before and after flippings and calculate the probability P. Then the r number between 0 and 1 is randomly generated. We accept the flip if $r < P$, accept the flip, conversely, reject the flip. The magnetization M of the system is

$$M = \frac{1}{N}\sum_{i=1}^{N}\boldsymbol{\mu}_i. \tag{9}$$

The flipping of all particles at a time is called one Monte Carlo steps (MCs). As in our previous work,[34] we used Gaussian adaptive sampling to increase the probability of flipping, namely adjust the sampling angle $\delta\theta$ according to the acceptance rate of the flip in each MCs. At each step, a particle is randomly selected and a new orientation is generated. On the basis of the original orientation, the new orientation change is less than the sampling angle $\delta\theta$. The energy difference between before and after flippings is then calculated, as well as the flip probability P. Finally, the probability P is used to determine whether or not to accept the sampling flip. We performed 10^5 MCs at each temperature and discarded the first 10^4 MCs (as the number of iterations required for the system to reach thermal equilibrium). Figure 6(a) shows the simulation results. There is a linear relationship between magnetization and temperature when L is less than 800 nm. However, it appears as though the magnetization curves at $L = 1000$ nm and $L = 1200$ nm are not linear, which could be explained by the large distance between adjacent particles, weakening the

interaction and similar paramagnetic behavior. Notably, we discovered a curve in the simulation curve that is extremely close to the experimental data, as illustrated in Fig. 6(b). There are 500 CuMnFe–PBAs clusters adsorbed on MWCNTs with a length of 700 nm in this example, corresponding to 0.089 CuMnFe–PBAs clusters per 1 nm × 1 nm area. At low temperatures, the abrupt increase in magnetization is attributed to the magnetic phase transition of CuMnFe–PBAs. The phase transition temperature decreases with decreasing size due to the finite size effect. The phase transition temperature in this system will be less than 5 K. Once the temperature exceeds 5 K, only a small amount of magnetization contributes to this system.

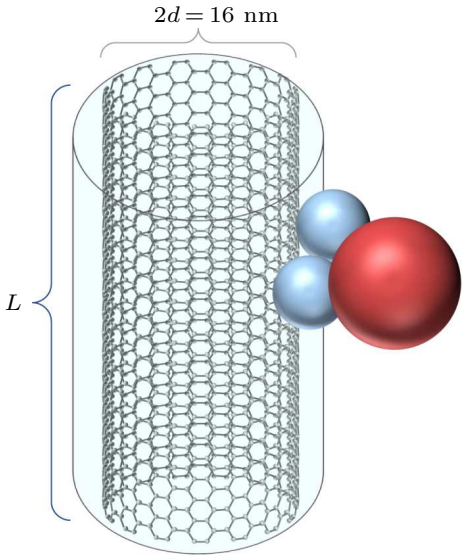


Fig. 5. The distribution space of CuMnFe–PBAs around the MWCNTs surface, reticular structure is MWCNT, and the blue space is the location of CuMnFe–PBAs clusters. When multiple particles are adsorbed on the surface of MWCNTs at the same time, there are some squeezed particles that can only be closely connected with neighboring particles, but not with the surface of carbon nanotubes. The gray part represents MWCNTs, blue balls are the CuMnFe–PBAs particles, and the red ball is the squeezed particles.

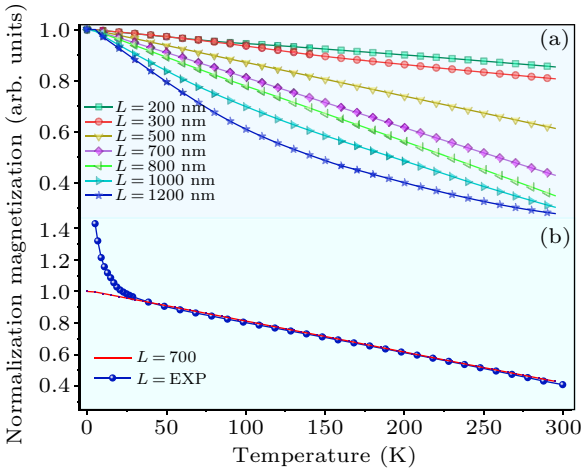


Fig. 6. (a) Simulated temperature-dependent normalization magnetization curve of CuMnFe–PBAs adsorbed on MWCNTs with different length L under magnetostatic interaction. (b) Comparison between the magnetization of measured CuMnFe–PBAs and the simulation results.

5. Conclusion

In summary, this work compared the properties of CuMnFe–PBAs and CuMnFe–PBAs@MWCNTs. CuMnFe–PBAs@MWCNTs exhibit a very unique magnetism compared to CuMnFe–PBAs, which is due to the size reduction (to less than 20 nm) caused by MWCNT adsorption. Additionally, we have determined the density of CuMnFe–PBAs adsorbed on the surface of MWCNTs using a magnetic simulation of magnetostatic interaction. The results indicate that 0.089 CuMnFe–PBAs clusters per 1 nm × 1 nm can be adsorbed onto the surface area of MWCNTs. This work provides a compelling explanation for why magnetization increases linearly with decreasing temperature and provides a comprehensive understanding of the adsorption mechanism of MWCNTs. This method will be used in future work on the adsorption of MWCNTs.

Acknowledgments

Project supported by the National Natural Science Foundation of China (Grant Nos. 11447231 and 12105137), the National Undergraduate Innovation and Entrepreneurship Training Program Support Projects of China, the Natural Science Foundation of Hunan Province, China (Grant No. 2020JJ4517), the Research Foundation of Education Bureau of Hunan Province, China (Grant Nos. 19A434, 19A433, and 19C1621), and the Opening Project of Cooperative Innovation Center for Nuclear Fuel Cycle Technology and Equipment, University of South China (Grant Nos. 2019KFY10 and 2019KFY09).

References

[1] Kunadian I, Andrews R, Mengüç M P and Qian D 2009 *Carbon* **47** 589
[2] Kunadian I, Andrews R, Qian D and Mengüç M P 2009 *Carbon* **47** 384
[3] Chen M L, Zhang F J and Oh W C 2009 *New Carbon Mater.* **24** 159
[4] Ramirez A P, Haddon R C, Zhou O, Fleming R M, Zhang, J, McClure S M and Smalley R E 1994 *Science* **265** 84
[5] Heremans J, Olk C H and Morelli D T 1994 *Phys. Rev. B* **49** 15122
[6] Likodimos V, Glenis S, Guskos N and Lin C L 2003 *Phys. Rev. B* **68** 045417
[7] Chang L W and Lue J T 2009 *J. Nanosci. Nanotechnol.* **9** 1956
[8] Husmann S, Nossol E and Zarbin A J G 2014 *Sensor Actuat. B-Chem.* **192** 782
[9] Gupta R and Singh B 2019 *J. Mater. Sci: Mater. El.* **30** 11888
[10] Kechrakos D and Trohidou K N 2003 *J. Magn. Magn. Mater.* **262** 107
[11] Ksenofontov V, Levchenko G, Reiman S, Gütlich P, Bleuzen A, Escax V and Verdaguer M 2003 *Phy. Rev. B* **68** 024415
[12] Moritomo Y and Shibata T 2009 *Appl. Phys. Lett.* **94** 043502
[13] Liu M, Lu Z, Ding X, Chen H, Guo Z, Hu S and Xiao J 2020 *Chem. Phys. Lett.* **754** 137641
[14] Goujon A, Varret F, Escax V, Bleuzen A and Verdaguer M 2001 *Polyhedron* **20** 1347
[15] Martinez-Garcia R, Knobel M and Reguera E 2006 *J. Phys. Chem. B* **110** 7296
[16] Tokoro H and Ohkoshi S I 2013 *Handbook of Nano-Optics and Nanophotonics* p. 693
[17] Shimamoto N, Ohkoshi S I, Sato O and Hashimoto K 2002 *Inorg. Chem.* **41** 678

[18] Yusuf S M, Kumar A and Yakhmi J V 2010 *J. Phys.: Conf. Ser.* **200** 022073
[19] Yusuf S M, Kumar A and Yakhmi J V 2009 *App. Phys. Lett.* **95** 182506
[20] Lahiri D, Choi Y, Yusuf S M, Kumar A, Ramanan N, Chattopadhyay S and Sharma S M 2016 *Mater. Res. Express* **3** 036101
[21] Zhang W, Wei X, Zhang X, Huo S, Gong A, Mo X and Li K 2022 *Sep. Purif. Technol.* **287** 120483
[22] Gao F, Zou J, Zhong W, Tu X, Huang X, Yu, Y and Bai L 2020 *Nanotechnology* **32** 085501
[23] Li J, Qiu J D, Xu J J, Chen H Y and Xia X H 2007 *Adv. Funct. Mater.* **17** 1574
[24] Okpalugo T I T, Papakonstantinou P, Murphy H, McLaughlin J and Brown N M D 2005 *Carbon* **43** 153
[25] Meiklejohn W H and Bean C P 1956 *Phys. Rev.* **102** 1413
[26] Chattopadhyay S, Jana S, Giri S and Majumdar S 2012 *J. Phys.: Condens. Mater* **24** 436005
[27] Mitra A, Mahapatra A S, Mallick A and Chakrabarti P K 2017 *J. Magn. Magn. Mater.* **435** 117
[28] Rondinone A J, Samia A C and Zhang Z J 1999 *J. Phys. Chem. B* **103** 6876
[29] Binns C, Maher M J, Pankhurst Q A, Kechrakos D and Trohidou K N 2002 *Phy. Rev. B* **66** 184413
[30] Iannotti V, Adamiano A, Ausanio G, Lanotte L, Aquilanti G, Coey J M D and Tampieri A 2017 *Inorg. Chem.* **56** 4446
[31] Nedelkoski Z, Kepaptsoglou D, Lari L, Wen T, Booth R A Oberdick, S D and Lazarov V K 2017 *Sci. Rep.* **7** 45997
[32] Mo J, Xia P, Zhang Q, *et al.* 2022 *Phy. Rev. B* **105** 094411
[33] Mo J, Zhang Q, Chen Y, Liu L, Xia P, Yang J and Liu M 2022 *J. Supercond. Nov. Magn.* **35** 1207
[34] Zhang Q, Mo J, Xie Y, Xia Y and Liu M 2022 *Phase Transit.* **95** 345